Volume 1 | Number 1 | Jan 2013 | Pages 1–100

Journal of
Materials Chemistry A

Materials for energy and sustainability
www.rsc.org/materialsA

Li⁺

ROYAL SOCIETY
OF CHEMISTRY

ROYAL SOCIETY
OF CHEMISTRY

www.rsc.org/materialsA

Highly defective CeO$_2$ as a promoter for efficient and stable water oxidation

Fengli Liang, Ying Yu, Wei Zhou,* Xiaoyong Xu, Zhonghua Zhu,*

A highly defective CeO$_2$ supported RuO$_2$ as electrocatalyst shows improved OER activity and stability in alkaline media.   This improvement is likely originating from the highly oxidative oxygen species O$_2^{2-}$/O$^-$ formed in the defective CeO$_2$ can easily migrate from CeO$_2$ and "spillover" to the surface of RuO$_2$ during OER process.

Journal of Materials Chemistry

Journal of Materials Chemistry A Accepted Manuscript

ARTICLE
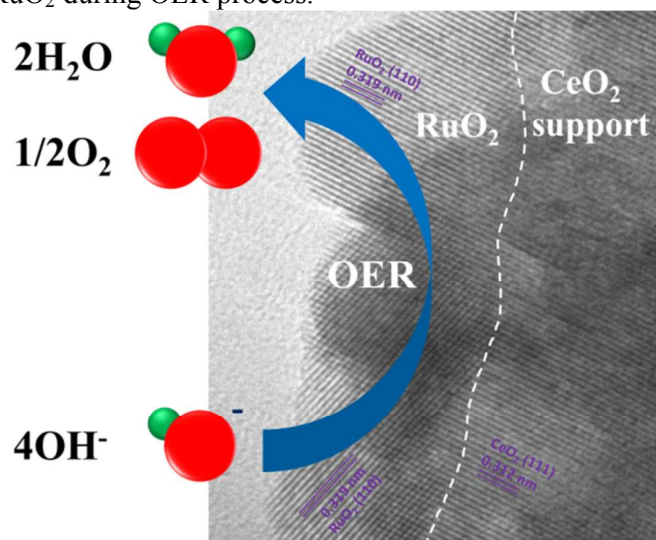
Highly defective CeO$_2$ as a promoter for efficient and stable water oxidation

Fengli Liang,[a] Ying Yu,[b] Wei Zhou, [a,*] Xiaoyong Xu,[a] Zhonghua Zhu[a,*]

Water oxidation is a critical step in water splitting to make hydrogen fuel. RuO$_2$ is one of the most active anode oxides for oxygen evolution reaction (OER). However, RuO$_2$ is very expensive and unstable in alkaline water electrolysis conditions. Here, we report a CeO$_2$ supported RuO$_2$ as highly efficient electrocatalyst for OER in alkaline media. We fabricated nano-sized CeO$_2$ particles by an "explosion" reaction using Ag@CeO$_2$ core-shell nanospheres as the precursor. High resolution transmission electron microscopy and Raman spectroscopy reveal the obtained CeO$_2$ particles possess a large number of oxygen defects. We decorated the defective CeO$_2$ with nano-sized RuO$_2$ (3-5 nm) through wet impregnation. The OER activity of RuO$_2$ is improved by ~150% on the defective CeO$_2$ as compared to the pristine RuO$_2$ electrocatalyst. Moreover, the RuO$_2$ supported on defective CeO$_2$ shows better stability in 0.1 M KOH electrolyte. The improved activity and stability are likely originating from the highly oxidative oxygen species O$_2^{2-}$/O$^-$ formed in the defective CeO$_2$, which can easily migrate from CeO$_2$ and "spillover" to the surface of RuO$_2$ during OER process.

1. Introduction

The electrolysis of water is an effective route for the large volumes of hydrogen gas production, which is the basis of long term renewable energy conversion and storage option. However, the efficiency of water electrolysis is limited by the large anodic overpotential of the oxygen evolution reaction (OER) [1, 2]. Great efforts have been devoted to the development of anode materials, such as precious metals, perovskite oxides and metal oxides, over the last decades to obtain practically useful OER rates at a lower overpotential with the aim of optimizing the overall electrolysis process [3-7].

Ruthenium oxide (RuO$_2$) is among the most active electrocatalysts reported to date for OER in water oxidation due to its wide potential window, reversible redox reaction and high electrical conductivity (300 S/cm) [2, 8-10]. Since their high cost and scarcity, synthesis of RuO$_2$ nanoparticles (NPs) with high specific surface area has been studied to minimize the usage [11-13]. However, it is still a challenge to use RuO$_2$ NPs because of its poor cycling ability and deteriorated performance caused by the higher-valent ruthenium oxides formed during OER [9, 14].

Cerium oxide (CeO$_2$) is a technologically important material due to its wide utilization in the field of environment catalysis, in three-way catalysts, low-temperature water-gas shift reaction, oxygen sensors, oxygen permeation membrane systems, and as catalyst supports. Traditional nanostructured design of cerium oxide catalysts typically focuses on their shape, size, and elemental composition [15-20]. As a matter of fact, the inherent defects (vacancy clusters) in CeO$_2$ are responsible for the enhancement of heterogeneous catalytic activity of CeO$_2$ supported catalysts, because the formation of more desired oxygen vacancy clusters will enhance cerium redox

ability [20-24]. Here, for the first time, we report an alternative way to improve the OER activity and stability of RuO$_2$ by supporting RuO$_2$ on highly defective CeO$_2$, although the CeO$_2$ itself (with or without oxygen vacancy clusters) is a poor oxide for OER.

2. Experimental Section

2.1 Synthesis of Materials

The Ag@CeO$_2$ core-shell spheres were prepared as the precursor of the highly defective CeO$_2$ by a co-precipitation method. The synthesis process of nano-structured highly defective CeO$_2$ is shown in Figure 1. 0.05 mol cerium (III) nitrate, 0.1 mol silver (I) nitrate and aqueous ammonia (0.25 mol NH^{3+}) were mixed into aqueous solution. The mixture was stirred and heated at 120 ºC for 4 h, and then reddish brown powders were obtained after filtration, washing and drying. The powders were calcined to form Ag@CeO$_2$ core-shell spheres at 600 ºC for 2 h. Excess concentrated HNO$_3$ (6 mol L^{-1}) was added to the Ag@CeO$_2$ core-shell spheres to form AgNO$_3$, NO, H$_2$O and CeO$_2$, followed by repeated washing and infiltration to obtain the defective CeO$_2$. The CeO$_2$ shell was decomposed into nanoparticles through an explosion process due to the dramatic emission of NO gas. The AgNO$_3$ solution can be recycled in large scale synthesis.
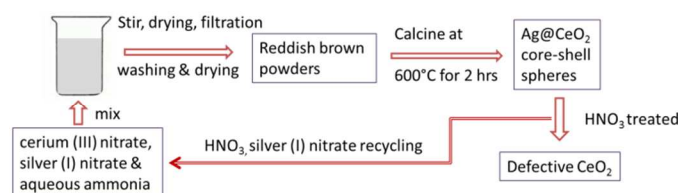
Figure 1. The synthesis process of highly defective CeO₂ nano-particles.

For comparison, we used a process similar to the preparation of Ag@CeO₂ to synthesize regular CeO₂ nano-particles without using AgNO₃. The synthesized CeO₂ particles possess no special morphology due to the absence of AgNO₃. The CeO₂ was also treated in 6M HNO₃ to rule out the possible effect from HNO₃. Even though tiny number of defects may form in these CeO₂, we call them non-defective CeO₂ in this study to make a contrast to the highly defective ones.

The deposition of nano-sized RuO_2 on CeO₂ was carried out through wet impregnation and pyrolysis. $RuCl_3$ was dissolved in acetone to obtain a solution of 2 mg mL^{-1}. A 450 mg mass of CeO₂ was added to the 39-mL $RuCl_3$ solution followed by sonication for 100 min. After the ultrasonic treatment the mixture was stirred at room temperature until the acetone evaporated. Acetone was selected as the solvent because acetone has a low surface tension (26 mN/m) [25]. The $RuCl_3$/CeO₂ samples were heated at 330ºC with heating rate of 1ºC min^{-1} in air to get fully oxidized RuO_2/CeO₂.

2.2 Materials Characterization

Powder X-ray diffraction (XRD) analysis was utilized to identify the crystallite structures of synthesized powders at room temperature and was performed on a Bruker D8 Advance instrument using monochromator-filtered Cu-Kα radiation at 40 kV. The data were collected in a step-scan mode in the range of 20-90° with intervals of 0.01° at a scanning rate of 1° min^{-1}. Le Bail refinements of the XRD patterns were performed using DIFFRACplus Topas 4.2 software. During the refinements, general parameters, such as the scale factor, background parameters, and the zero point of the counter, were optimized. Transmission electron microscopy (TEM) was performed at 200 kV on a field-emission instrument of type JEOL JEM-2100F. The morphology of the material was studied by FESEM (JEOL 7001) with an embedded energy dispersive X-ray spectroscopy (EDS) system. The surface composition and chemical state of Ru and O was analyzed by XPS (Kratos Axis ULTRA). Raman spectra were recorded in the backscattering mode at room temperature on a Renishaw inVia micro-Raman system equipped with an optical microscope comprising a 50× objective lens. N₂ physisorption was performed at 77 K on Micromeritics TriStar II 3020, after degassing the samples for 12 h at 120 °C before test. Total specific surface areas were determined according to Brunauer-Emmett-Teller (BET) method.

2.3 Electrochemical Characterization

CeO₂, RuO_2 and RuO_2/CeO₂ electrocataysts were mixed with as-received carbon (Super C65) from TIMCAL C'NERGY at a 1:1 mass to remove any electronic conductivity limitations within the thin film electrodes. The electrocatalyst suspension was prepared by sonication of electrocatayst (10 mg), carbon (10 mg), ethanol (1 mL) and Nafion solution (5 wt %, 100 μL) for 30 min. An aliquot of 5 μL of suspension was drop-casted onto a glassy carbon disk electrode (4 mm diameter, 0.126 cm² area) and left to dry under a glass jar. The loading of the CeO₂, RuO_2 or RuO_2/CeO₂ electrocatalyst onto glassy carbon surface was about 360 μg cm^{-2}.

Voltammetric experiments were performed with a Biologic VMP2/Z multichannel potentiostat. Linear sweep voltammograms (LSV) was performed on a rotating disk electrode (RDE) and obtained in an O₂ (99.999%) saturated 0.1 M KOH solution with a scan rate of 10 mV s^{-1} at room temperature using a platinum wire counter electrode and a Ag|AgCl (3M NaCl) reference electrode, which was calibrated with respect to reversible hydrogen electrode (RHE). All the potentials in this study are *iR*-corrected potentials to compensate for the effect of solution resistance, which were calculated by the following equation:

$$E \text{ (}iR\text{-corrected)} = E\text{-}iR$$

Where *i* is the current and *R* is the uncompensated ohmic electrolyte resistance measured via high frequency ac impedance in O₂-saturated 0.1 M KOH.

3. Results and Discussion

In our previous study, we found that large number of defects can be formed in CeO₂ in the Ag@CeO₂ core-shell nanoparticles prepared by a one-pot surfactant-free redox method [26]. In order to remove Ag and obtain CeO₂ nano-particles, concentrated HNO₃ was added to Ag@CeO₂ to trigger an "explosion" reaction, during which the CeO₂ shell was decomposed into smaller grains and the Ag was removed. We tried HNO₃ with different concentration to react with Ag@CeO₂ for 10 minutes to confirm the formation mechanism of CeO₂ nanopaticles. As can be seen from TEM images, the sphere structure of CeO₂ shell was only partially destroyed by 0.1 mol L^{-1} of HNO₃ (Figure 2a), while it was decomposed into CeO₂ hemispheres when 1 mol L^{-1} of HNO₃ was used (Figure 2b). The even smaller CeO₂ nano-particles were obtained by increasing the concentration of HNO₃ to 6 mol L^{-1} (Figure 2c). In order to rule out the possible corrosive impact of HNO₃ on the connection between CeO₂ grains, the CeO₂ hemispheres were treated in 6 mol L^{-1} of HNO₃. After the treatment, the CeO₂ hemispheres retained their morphology. Based on these results, we confirm the CeO₂ nanoparticles formed through the explosion process due to the dramatic emission of NO gas as schematically shown in Figure 2d. The absence of Ag in defective CeO₂ catalyst was confirmed by XPS survey scan as shown in Figure S1.
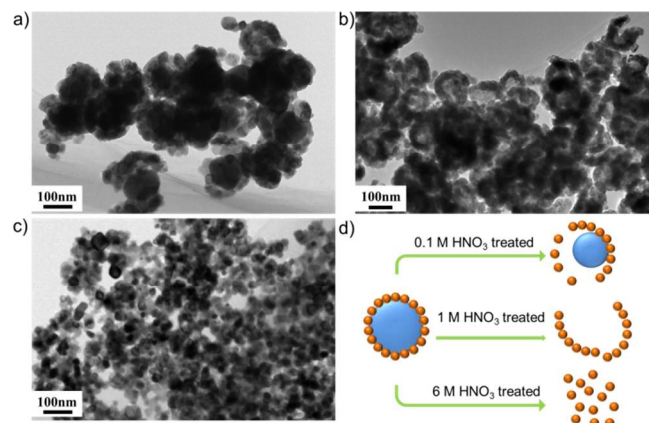
Figure 2. TEM images of Ag@CeO₂ after treatment in different concentrated HNO₃: (a) 0.1 mol L^{-1}, (b) 1 mol L^{-1}, and (c) 6 mol L^{-1}. The schematic of the formation mechanism of CeO₂ nano-paticles (d).

Figure 3 shows the Raman spectra of defective and non-defective CeO₂. The non-defective CeO₂ powders were also treated in 6M HNO₃ to rule out the possible effect from HNO₃. The defective CeO₂ shows additional peak at around 560 cm^{-1}, which is an indicative of the creation of massive number of oxygen vacancies clusters in CeO₂

[15, 21]. It has been reported that the oxygen vacancy clusters can promote the catalytic activity of ceria due to the improved redox properties of Ce^{4+}/Ce^{3+} [20, 27-29].

Figure 4 shows the comparison of high-resolution TEM images of the defective and non-defective CeO_2. The perfect lattice is observed in non-defective CeO_2, while many "dark pits" are observed in the defective CeO_2. This revealed the surface of the defective CeO_2 was rougher than that of non-defective ones. Appearance of these dark pits is likely due to the formation of oxygen vacancies clusters in CeO_2 [27].
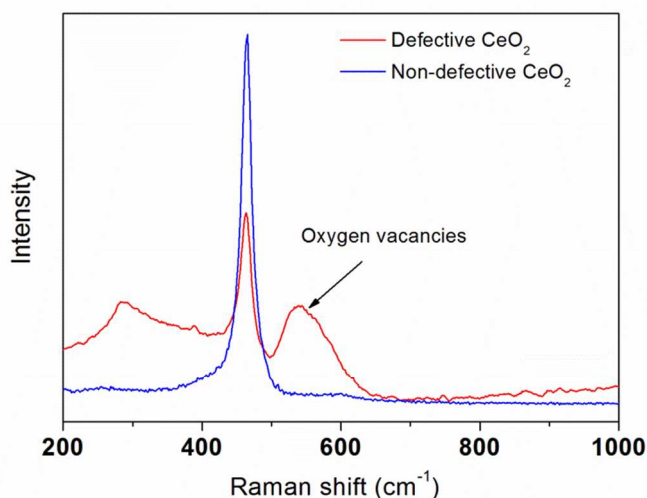
XPS spectra for both samples present two features at about 529 and 531 eV. The lower binding energy peak can be ascribed to the lattice oxygen species (O^{2-}) and the higher one can be assigned to less electron-rich oxygen species. By deconvoluting the broad peak at higher binding energy, both samples can be deconvoluted in three peaks: the one with lower BE (530.5 eV) is assigned to oxygen in the form of O_2^{2-}/O^- on the surface; the next (531.6 eV) is ascribed to the hydroxyl groups (-OH) or the surface-adsorbed oxygen (O_2); and the third peak (533 eV) is due to molecular water or carbonates adsorbed on the surface [30]. The possibility of appearance of carbonates on the surface of CeO_2 can be ruled out because no vibrational peaks belong to $-CO_3^{2-}$ was detected by Raman and FT-IR. **Table 1** lists the relative concentrations of the different kinds of oxygen species which are estimated from the relative area of these subpeaks. As can be seen, the relative concentration of O_2^{2-}/O^- is much higher in defective CeO_2.

Figure 3. Raman spectra of defective and non-defective CeO_2.

Table 1. O1s XPS Peak Deconvolution Results

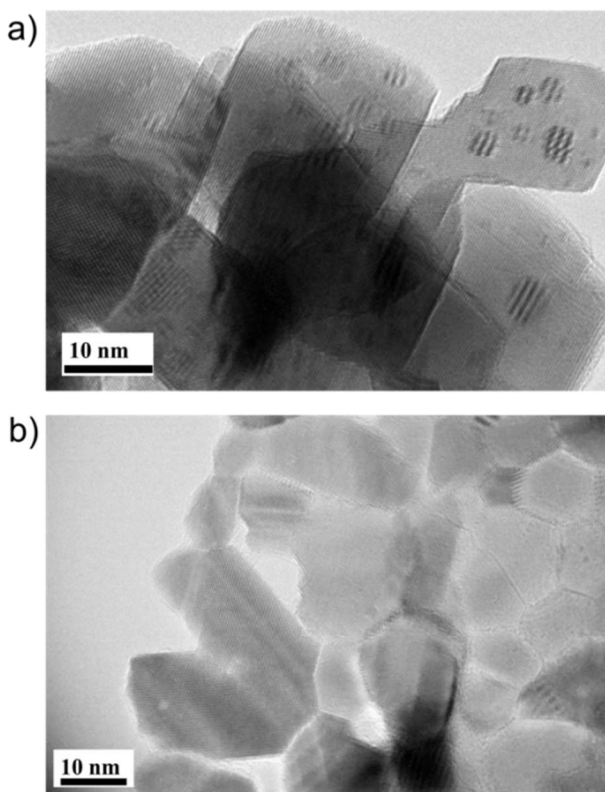| Samples	O^{2-}	O_2^{2-}/O^-	$-OH/O_2$	H_2O
Defective CeO_2	73.71	12.68	8.79	4.83
Non-defective CeO_2	84.62	1.34	10.42	3.63

Figure 4. The TEM images of (a) defective and (b) non-defective CeO_2.

The oxygen species on the two CeO_2 samples are probed by XPS. The XPS spectra of the O1s levels are shown in Figure 5. The O1s
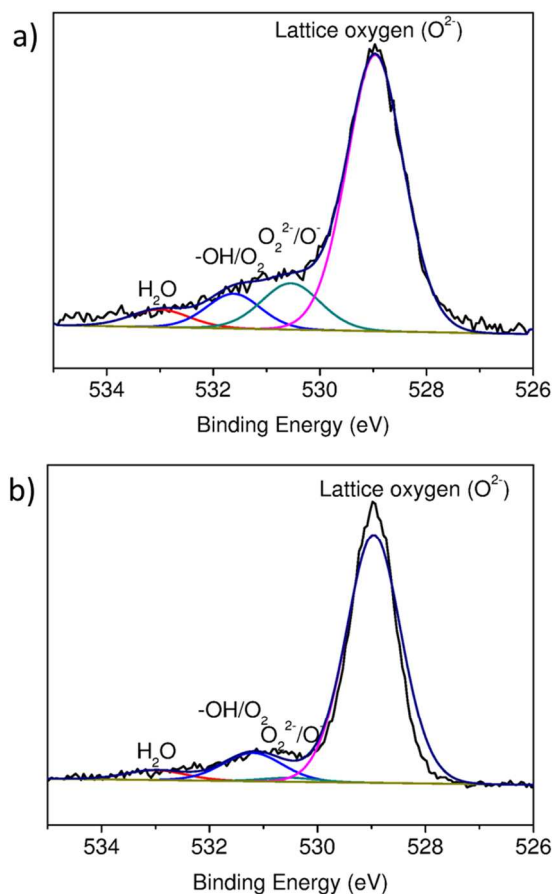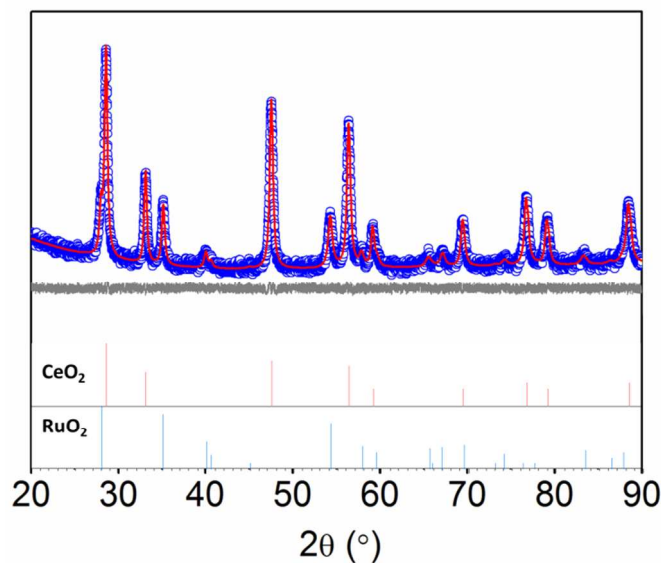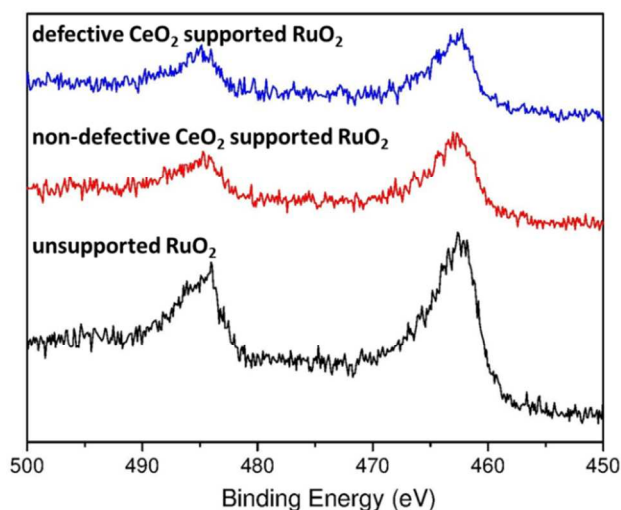

Figure 5. XPS spectrum of the O1s levels of (a) defective and (b) non-defective CeO_2.
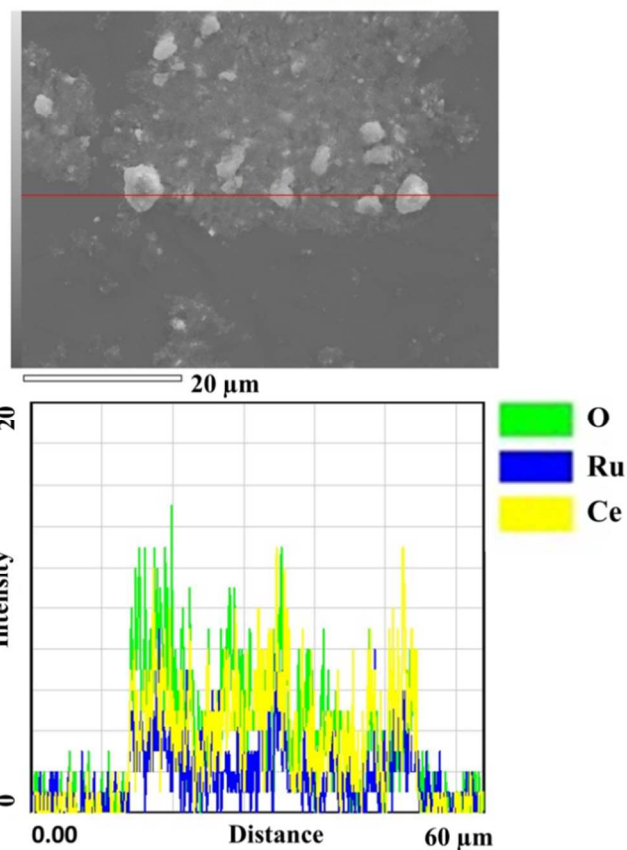
Figure 6. X-ray diffraction profile of the defective CeO_2 supported RuO_2 composite. Observed (blue circles), calculated by the Rietveld method (red line), difference (grey line) and calculated Bragg positions (vertical bars) for RuO_2 and CeO_2 phases are presented.

XRD analysis was conducted after the RuO_2 catalysts were deposited onto the surface of the defective CeO_2. Figure 6 shows the XRD pattern of defective CeO_2 supported RuO_2 composite. The Le Bail refinement reveals the formation of well crystalized fluorite-type CeO_2 and rutile-type RuO_2 with Fm-3m (a=5.415997(5) Å) and $P4_2$/mnm space group (a=b=4.511724(4) Å; c=3.103031(1) Å) respectively. Table S1 listed the detailed structure parameters for the two phases. The reliability of the refinement is R_p=3.75 %, R_{wp}=4.74 %, and χ^2=1.08. The binding energy of Ru3p was measured with XPS and compared in Figure 7. The two CeO_2 supported RuO_2 samples show lower intensity due to the lower Ru loading content relative to the pristine RuO_2 sample. The peak position for Ru $3p_{3/2}$ is around 462.5 eV for the supported RuO_2 samples and pristine RuO_2, indicating the formation of Ru^{IV} [14] in the composite (Figure 7).
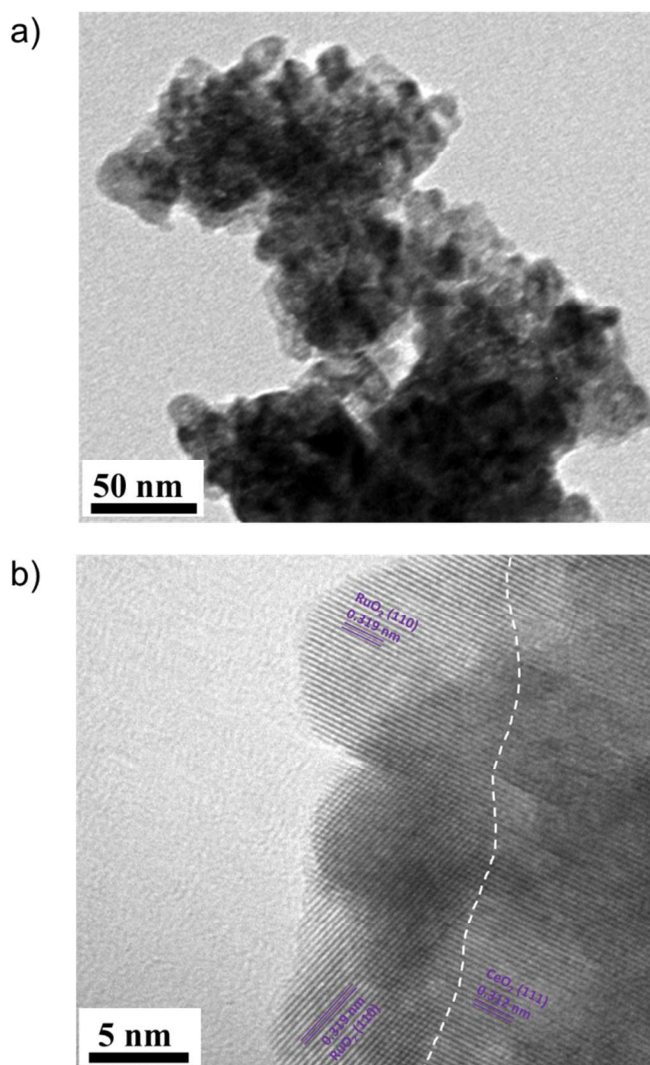

Figure 8. The SEM image of the defective CeO_2 supported RuO_2 together with the elemental line analysis by EDS.

Figure 8 shows the SEM image of the defective CeO_2 supported RuO_2 together with the elemental line analysis by EDS. The RuO_2 particles are too small to be identified by SEM, but the EDS result presents that Ru and Ce elements distribute homogenously along the scanning line indicating the uniformly distribution of RuO_2 on CeO_2. To gain the morphology of the RuO_2, the sample was studied by TEM. Compared with the TEM image of the pure defective CeO_2 (Figure 2c), additional tiny grains were found wrapped on the CeO_2 (Figure 9a). Figure 9b is the corresponding HRTEM image of RuO_2 nano-grains (5~8 nm) and shows the d[110] spacing of 0.319 nm, which matches well with the XRD results (Table S1). Combining the XRD with XPS analysis we can conclude these smaller particles are RuO_2.

Figure 7. XPS of Ru3p in the defective CeO_2 supported RuO_2 catalysts, non-defective CeO_2 supported and pristine RuO_2.

Figure 9. TEM image of the defective CeO_2 supported RuO_2 composite and different magnifications.

The OER activity of the prepared electrocatalysts is evaluated on a glass carbon electrode, where a thin-film of CeO_2 supported RuO_2 mixed with carbon and Nafion was deposited. Figure 10a compares the cyclic voltammograms (CV) measurement of the defective CeO_2 supported RuO_2 catalysts, non-defective CeO_2 supported and pristine RuO_2 in O_2-saturated 0.1 M KOH. The current density of the OER is normalized to the mass of the RuO_2 loading. The redox couple peaks of $Ru^{VI/VII}$ at 1.35 V vs RHE [31] can be observed for the pristine RuO_2, while the oxidation peak of $Ru^{VI/VII}$ is broaden for non-defective CeO_2 supported RuO_2. It is interesting that the oxidation peak of $Ru^{VI/VII}$ is absent for defective CeO_2 supported RuO_2. Instead, additional anodic and cathodic peaks appear in the CV curve of defective CeO_2 supported RuO_2, which are not observed for the non-defective CeO_2 supported and pristine RuO_2. These additional peaks are related to the high redox nature of the highly defective CeO_2 (Supporting information, Figure S2). It is noteworthy that CeO_2 itself is a poor OER electrocatalyst even with high defects (Supporting information, Figure S2). Linear sweep voltammograms of three samples are shown in Figure 10b. The non-defective CeO_2 supported and pristine RuO_2 show very similar activity indicating non-defective CeO_2 has negligible effect on the OER activity of

RuO_2; while the OER activities of the defective CeO_2 supported RuO_2 were improved by a factor of 2.38~2.45 at overpotential (η) of 0.3 and 0.4V (Figure 10c). The specific surface areas for the defective CeO_2 and non-defective CeO_2 powders are 16.4 and 31.5 $m^2\ g^{-1}$, respectively. Despite a larger surface area, the non-defective CeO_2 supported RuO_2 shows lower activity than the defective CeO_2 supported one. This clearly demonstrates that the defects in CeO_2 play a dominant role in controlling the OER activity.
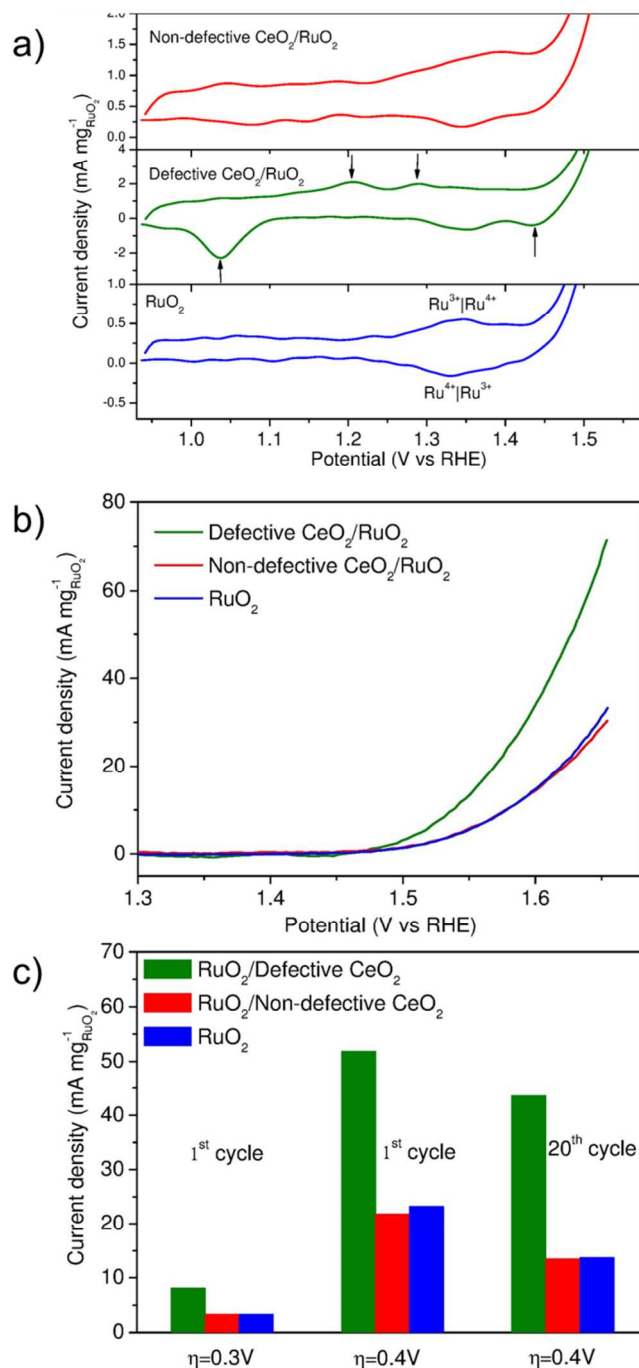
Figure 10. Cyclic voltammograms (CV) measurement (a), linear sweep voltammograms (b), the mass activity and stability at overpotential (η) of 0.3 and 0.4V (c) of the defective CeO_2 supported RuO_2 catalysts, non-defective CeO_2 supported and pristine RuO_2 in O_2-saturated 0.1 M KOH.

The Ru*3p* lines show negligible difference for all the samples (Figure 7), indicating the different OER activity is not originating from the RuO_2 itself. It has been reported that the clusters of more than two vacancies, such as linear surface oxygen vacancies, are favorable for migration of oxygen [27, 28]; and the oxygen species can migrate fast on the surface of RuO_2 under the polarization through spillover effect [32]. Therefore, it is likely that the highly oxidative oxygen species O_2^{2-}/O^- formed in the defective CeO_2 can easily migrate from CeO_2 and "spillover" to the surface of RuO_2 during OER process to promote the oxidation of water.

It has been reported that RuO_2 is unstable in alkaline solution during the OER process [10], which was also the case for all the three samples in our study. However, the degradation of activity of the defective CeO_2 supported RuO_2 is alleviated relative to the non-defective CeO_2 supported RuO_2 and pristine RuO_2 (Figure 10c). After 20 cycles measurement the activity degradation rate is 16% for the defective CeO_2 supported RuO_2 at η=0.4V, which is less than the degradation of 38% and 41% for the non-defective CeO_2 supported RuO_2 and the pristine RuO_2 respectively. This suggests that the CeO_2 support can improve the stability of the RuO_2 and this improvement is more remarkable at the presence of large number of defects in CeO_2. It is possible that the O_2^{2-}/O^- species can suppress the oxidization of Ru to very high valence during the OER process. This view can be supported by the absence of $Ru^{VI/VII}$ oxidation peak during the anodic scan on defective CeO_2 supported RuO_2 (Figure 10a). The effect of oxygen vacancy concentration of support on the stability of RuO_2 is ongoing in our group.

4. Conclusions

In summary, we synthesized nano-sized highly defective CeO_2 through an "explosion" reaction using Ag@CeO_2 core-shell nano-spheres as precursors. CeO_2 supported RuO_2 composite electrocatalysts were fabricated by wet impregnation. OER activities of the defective CeO_2 supported RuO_2 were improved by a factor of 2.38~2.45 at overpotential (η) of 0.3 and 0.4V relative to the pristine RuO_2. Moreover, the defective CeO_2 support also improved the stability of the RuO_2. It is likely that the highly oxidative oxygen species O_2^{2-}/O^- formed in the defective CeO_2 can easily migrate from CeO_2 and "spillover" to the surface of RuO_2 during OER process to facilitate the water oxidation.

Notes and references

a   School of Chemical Engineering, The University of Queensland, Brisbane, Queensland 4072, Australia.

*Corresponding author. E-mail: z.zhu@uq.edu.au (Z H Zhu) or wei.zhou@uq.edu.au (W Zhou), Fax: 61 7 3365 4199; Tel: 61 7 33653528

b   Centre for Microscopy and Microanalysis, University of Queensland Brisbane, Queensland 4072, Australia.

[1]   L. Trotochaud, J. K. Ranney, K. N. Williams, S. W. Boettcher, J. Am. Chem. Soc. **2012**, *134*, 17253–17261.

[2]   M. E. G. Lyons, S. Floquet, Phys. Chem. Chem. Phys. **2011**, *13*, 5314–5335.

[3]   W. Zhou, J. Sunarso, J. Phys. Chem. Lett. **2013**, *4*, 2982-2988.

[4]   M. E. G. Lyons, M. P. Brandon, Phys. Chem. Chem. Phys. **2009**, *11*, 2203-2217.

[5]   D. Cibrev, M. Jankulovska, T. Lana-Villarreal, R. Gomez, Int. J. Hydrogen Energy **2013**, *38*, 2746-2753.

[6]   M. Gong, Y. Li, H. Wang, Y. Liang, J. Z. Wu, J. Zhou, J. Wang, T. Regier, F. Wei, H. Dai, J. Am. Chem. Soc. **2013**, *135*, 8452-8455.

[7]   Y. Cheng, C. Liu, H. M. Cheng, S. P. Jiang, Appl. Mater. Interfaces **2014**, *6*, 10089-10098.

[8]   G. Wang, L. Zhang, J. Zhang, Chem. Soc. Rev. **2012**, *41*, 797–828.

[9]   A. S. Kelsey, Q. Liang, D. B. Michael, Y. Shao-Horn, J. Phys. Chem. Lett. **2014**, *5*, 1636-1641.

[10]   E. Guerrini, S. Trasatti, Russ. J. Electrochem. **2006**, *42*, 1017-1025.

[11]   J. Jirkovský, H. Hoffmannová, M. Klementová, P. Krtil, J. Electrochem. Soc. **2006**, *153*, E111-E118.

[12]   J. Jirkovský, M. Klementová, P. Krtil, Electrochem. Commun. **2006**, *8*, 1417-1422.

[13]   Y. M. Lee, J. Suntivich, K. J. May, E. E. Perry, Y. Shao-Horn, J. Phys. Chem. Lett. **2012**, *3*, 399-404.

[14]   R. Kötz, H. J. Lewerenz, S. Stucki, J. Electrochem. Soc. **1983**, *130*, 825-829.

[15]   Z. L. Wu, M. J. Li, J. Howe, H. M. Meyer III, S.H. Overbury, Langmuir **2010**, *26*, 16595-16606.

[16]   A. S. Ivanova, Kinet. Catal. **2009**, *50*, 797-815.

[17]   C. Binet, M. Daturi, J. C. Lavalley, Catal. Today **1999**, *50*, 207-225.

[18]   C. L. Campos, C. Roldan, M. Aponte, Y. Ishikawa, C. R. Cabrera, J. Electroanal. Chem. **2005**, *581*, 206-215.

[19]   E. P. Murray, T. Tsai, S. A. Barnett, Nature **1999**, *400*, 649-651.

[20]   N. J. Lawrence, J. R. Brewer, L. Wang, T. S. Wu, J. Wells-Kingsbury, M. M. Ihrig, G. H. Wang, Y. L. Soo, W. N. Mei, C. L.Cheung, Nano Lett. **2011**, *11*, 2666-2671.

[21]   T. Taniguchi, T. Watanabe, N. Sugiyama, A. K. Subramani, H. Wagata, N. Matsushita, M. Yoshimura, J. Phys. Chem. C **2009**, *113*, 19789-19793.

[22]   B. Murugan, A. V. Ramaswamy, J. Am. Chem. Soc. **2007**, *129*, 3062-3063.

[23]   J. Guzman, S. Carrettin, A. Corma, J. Am. Chem. Soc. **2005**, *127*, 3286-3287.

[24]   S. Agarwal, X. Zhu, E. J. M. Hensen, L. Lefferts, B. L. Mojet, J. Phys. Chem. C **2014**, *118*, 4131-4142.

[25]   L. Wang, L. Ge, T. E. Rufford, J. L. Chen, W. Zhou, Z. H. Zhu, V. Rudolph, Carbon 2011, 49, 2022-2032.

[26]   F. L. Liang, W. Zhou, Z. H. Zhu, ChemElectroChem DOI: 10.1002/celc.201402143

[27]   X. Liu, K. Zhou, L. Wang, B. Wang, Y. Li, J. Am. Chem. Soc. **2009**, *131*, 3140-3141.

[28]   C. W. Sun, H. Li, L. Q. Chen, Energy Environ. Sci. **2012**, *5*, 8475-8505.

[29]   F. Esch, S. Fabris, L. Zhou, T. Montini, C. Africh, P. Fornasiero, G. Comelli, R. Rosei, Science **2005**, *309*, 752-755.

[30]   Y. G. Wang, J. W. Ren, Y. Q. Wang, F. Y. Zhang, X. H. Liu, Y. Guo, G. Z. Lu, J. Phys. Chem. C **2008**, *112*, 15293-15298.

[31]   S. Trasatti, Electrochim. Acta **1984**, *29*, 1503-1512.

[32]   S. Wodiunig, F. Bokeloh, J. Nicole, C. Comninellis, Electrochem. Solid-State Lett. **1999**, *2*, 281-283.

.